Microstructural changes induced in advanced tungsten grades under high temperature neutron irradiation

W. Van Renterghem [a],[*], K. Iroc [a],[b], D. Terentyev [a], S. Antusch [c], M. Rieth [c]

[a] *SCK CEN, Nuclear Energy and Technology Institute, Boeretang 200, B-2400 Mol, Belgium*
[b] *EMAT, Department of Physics, University of Antwerp, Groenenborgerlaan 171, 2020 Antwerpen, Belgium*
[c] *Karlsruhe Institute of Technology (KIT), Institute for Applied Materials, 76344 Eggenstein-Leopoldshafen, Germany*

ARTICLE INFO

ABSTRACT

Recent studies addressing the change of mechanical properties after high temperature irradiation of tungsten have reported substantial increase of the ductile to brittle transition temperature as well as increase of the hardness. In this work, we performed microstructural analysis by means of transmission electron microscopy (TEM) on various tungsten grades earlier exposed to high temperature neutron irradiation at 1200 °C up to 1 dpa. The latter corresponds to the expected irradiation temperature on the surface of a tungsten monoblock during the steady state operation in ITER. TEM was applied to five tungsten (W) materials including ITER specification pure W and precipitate strengthened W alloys. The analysis of TEM data coupled with its discussion led to a number of important conclusions regarding the damage induced at 1200 °C neutron irradiation such as: (i) weak effect of recrystallization on the accumulation of the lattice damage; (ii) promising results on the tolerance of damage accumulation in W-Y_2O_3 grade and (iii) internal oxidation of TiC particles which may contribute to the huge increase of the irradiation induced hardening.

1. Introduction

Tungsten (W) is selected as armor material in fusion devices (i.e. JET, ITER, and candidate for DEMO applications [1–3]) because of its ability to withstand high heat loads, prolonged interaction with plasma and acceptable nuclear activation [3]. During the operation in the fusion environment, 14 MeV fast neutrons will penetrate the plasma facing components causing atomic displacement damage (measured in units of displacement per atom, dpa) and subsequent formation of structural lattice defects such as voids, dislocation loops and transmutation products [4–6]. The presence of those defects will suppress plastic deformation mechanisms which otherwise help to dissipate thermal stresses. Accordingly, upon the operation in a nuclear fusion environment the material is gradually converted from ductile into brittle state.

In the specific case of W, even in the non-irradiated state, the ductile-to-brittle transition temperature (DBTT) is rather high, being 300–400 °C [7,8]. Even though the main function of W is armor, it also includes a structural function in the current ITER divertor design [3,9]. Given the unavoidable degradation of W properties due to the irradiation, the design of the divertor components should account for the change of the mechanical properties after neutron irradiation. The modification of the microstructure due to the neutron irradiation in the hot part (i.e. close to the plasma surface) may result in the reduction of thermal conductivity as well as alter the trapping of tritium and helium coming from the plasma [6]. This was the incentive for the recent experimental studies addressing high temperature neutron irradiation (up to 1200 °C) and its effect on the mechanical properties such as change of hardness and DBTT [10–12]. The cited studies included both ITER specification tungsten products (produced by Plansee Austria and ALMT Japan) as well as particle strengthened W alloys (W-TiC and W-Y_2O_3) manufactured by innovative processing such as powder injection molding.

The hardening induced after 1200 °C irradiation up to ~1 dpa, assessed in these studies, have shown a number of important findings, namely: (i) the irradiation hardening in W-TiC is abnormally high compared to the other W grades which were irradiated face-to-face, the origin of which remains unclear; (ii) although the irradiation hardening at T_{irr} = 1200 °C is lower than at lower irradiation temperatures e.g. 600 °C and 1000 °C, it is by far not negligible and it amounts to about 30–60% of the reference hardness value. Thus, even at high irradiation temperature (T_m/3), the accumulation of irradiation defects in tungsten is apparently not suppressed by the thermally activated diffusion and

subsequent self-annihilation; (iii) the smallest irradiation hardening (i. e., the best resistance to the irradiation damage) is observed in materials with the highest density of sinks. However, in the case of 1200 °C irradiation, it is not clear whether thermally activated microstructural recovery would occur in the course of the irradiation (achieving 1 dpa in W in this experiment took about 125 days of irradiation). All the above listed observations explain the need for characterization of the microstructure after the high temperature irradiation.

Open literature contains several transmission electron microscopy (TEM) studies on various tungsten grades, exposed to neutron irradiation at high temperatures ($T_{irr} \geq 900$ °C) to establish relations between the irradiation-induced microstructure and the modification of the mechanical properties [11,13–16]. These studies typically focus on radiation-induced defects, such as dislocation loops, micro-voids and transmutation-induced precipitates. Several grades of tungsten were irradiated by neutrons at 600, 800 and 1200 °C and characterized by Dubinko et al. [11]. The highest irradiation temperature (1200 °C) resulted in the lowest dislocation loop and micro-void densities, attributed to absorption by defect sinks. However, micro-voids are more stable at high irradiation temperatures (1200 °C) and contribute more significantly to the hardness than the dislocation loops. In a TEM study by Papadakis et al. [16], a microstructural comparison was made between non-irradiated, as-forged tungsten annealed at 1200 °C and tungsten neutron-irradiated at 1200 °C. The study showed the formation of radiation-induced voids due to the diffusion of small vacancy clusters caused by the high irradiation temperature. Grain boundaries act as sinks for voids and have a denuded zone up to 30 nm wide. In addition to dislocation loops and voids, the presence and spatial distribution of transmutation elements, like Rhenium and Osmium, also contributes to radiation-induced hardening. To reveal the spatial distribution of transmutation elements, both single and polycrystalline pure tungsten samples were exposed to neutron irradiation at 900 °C and characterized by TEM [14]. The results revealed that Re segregates on voids and grain boundaries in polycrystalline tungsten, while it forms *Re*-rich precipitates throughout the lattice in single crystal tungsten. The irradiation temperature has a significant influence on the structure of the transmutation products. To investigate that, identical polycrystalline tungsten samples were exposed to neutron irradiation within a temperature range between 460 and 1100 °C [15]. The results showed that, the tungsten irradiated at 1100 °C contains acicular precipitates rich in Re and Os, indicating the stability at high temperature. However, at an irradiation temperature around 500 °C, Re and Os were distributed as nanoscale clusters, proving the dependence of the mobility of transmutation elements and their binding into specific phases on the irradiation temperature. Overall, the high temperature irradiation in tungsten still leads to progressive void formation and high density of precipitates, despite intensive thermal diffusion which should help to recover the irradiation induced defects, causing embrittlement and loss of thermal conductivity [17–19].

The above discussed knowledge covers the microstructure induced in pure tungsten. However, numerous efforts have been made over the last decade to improve properties of tungsten by alloying (see e.g. [20–25] and references therein). Accordingly, the investigation of the high temperature irradiation effects in those innovative materials is important for the validation of the thermal stability of the initial microstructure which was beneficial for the properties of those materials in the non-irradiated state. In addition, one also needs to explore up to which extent the formation of voids and transmutation precipitates pursues at high temperature irradiation in those tungsten alloys.

The present work aims at exploring the microstructural changes induced in several advanced tungsten grades, that were earlier exposed to 1200 °C neutron irradiation in the BR2 reactor [10] to a fluence comparable to the end of design life of ITER (i.e. 1 dpa). The materials can be categorized into two groups: commercially available tungsten conform with ITER specification and particle reinforced tungsten alloys. The three ITER specification tungsten materials include Plansee forged

bars in the conditions as-forged and as-recrystallized (at 1600 °C for one hour), and ITER specification tungsten rolled plate produced by A.L.M. T. The other two tungsten materials are particle reinforced grades: tungsten alloyed with 1 wt% of TiC, and tungsten alloyed with 2 wt% of Y_2O_3. A particular advantage of these W alloys is the fine grain size as well as superior resistance against recrystallization and grain growth achieved as a result of the stabilization of grain boundaries by the fine-scale precipitates. In view of the fine grain size and assuming that grain boundaries act as neutral sinks for the irradiation defects, the original expectation was to observe a better resistance of these materials against irradiation in terms of the increase of the hardness. Nevertheless, as it was shown by Yin et al. [26], the additional hardness induced by the 1200 °C irradiation turned out to be very high in W1TiC, much higher than any other of the tungsten grades irradiated face-to-face with W1TiC. On the other hand, the increase of the hardness in WY_2O_3 was the smallest of all investigated materials. This effect is illustrated in Fig. 1, which plots the radiation induced hardness increase as a function of irradiation temperature for each of the five alloys. Another unclear result of the previous study was a considerable difference in the irradiation hardness induced after 1200 °C in IGP and ALMT materials.

Given these unexpected results, the main objective of this study was to perform a thorough microstructural characterization by TEM to (i) assess the density and size distribution of loops and voids; (ii) reveal possible heterogeneities in the loop/void spatial distributions; (iii) characterize the background microstructure (dislocation density/sub-grain size) as much as the observation zone would allow; (iv) characterize the microstructure of the strengthening particles; (v) characterize the microstructure near the particle-matrix interface in the set of tungsten grades irradiated face-to-face at 1200 °C in [26].

2. Investigated materials and experimental procedures

2.1. Investigated materials

The basic information about the fabrication route of the studied materials is summarized below together with the acronyms used throughout this paper to refer to those materials:

IGP: Commercially pure ITER specification tungsten grade produced by Plansee, Austria. The material is supplied as a rod (with square cross-section 36 mm × 36 mm) which was hammered on both sides, more info
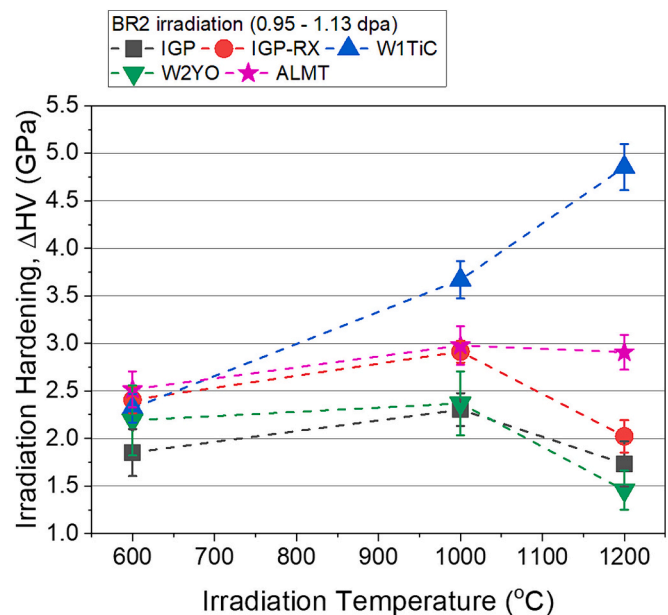

Fig. 1. Irradiation induced hardness in the investigated materials which was studied by Yin et al. [26].

on the properties of this material can be found in [27]. The material is studied in the as-fabricated stress-relived state.

IGP-RX: IGP material exposed to thermal annealing at 1600 °C for 1 h to induce the recrystallization. The recrystallized material is expected to occur in the upper part of the heat treated monoblock, from where a sample was extracted.

ALMT: Commercially pure ITER specification tungsten grade produced by A.L.M.T., Japan. The samples were cut from the mono-blocks. The material has microstructure and chemical composition very similar to what is reported by Nogami et al. [28].

W2YO: Pure tungsten doped with 2% Y_2O_3 particles, produced by powder injection molding and sintered at 2400 °C by Karlsruhe Institute of Technology, Germany.

W1TiC: Pure tungsten doped with 1% TIC particles, produced by powder injection molding and sintered at 2400 °C by Karlsruhe Institute of Technology, Germany.

Basic information on the material composition and grain size is provided in Table 1.

2.2. Irradiation conditions

Disk shaped specimens of 12 mm diameter and 0.5 mm thickness were irradiated in the Belgian Reactor 2 (BR2) at a temperature of 1200 °C. The specimens were placed in a steel capsule, which also acted as a shield for thermal neutrons. The capsule was filled with inert gas to prevent oxidation due to the high irradiation temperature. The accumulated fast neutron (E > 1 MeV) fluence was ~1.5 × 10^25 n/m^2 corresponding to a dose of 1.05 dpa, as calculated by the ALEPH code [29]. The same code was applied, using the accessible nuclear cross section databases [30–32], to calculate the amount of Re and Os emerging as a result of transmutation. The calculated concentrations of transmuted Re and Os at 1.05 dpa are 2.2 at.% and 0.25 at.%, respectively.

2.3. TEM investigation

Samples were prepared for TEM analysis with a ThermoFisher Scios dual beam focused ion beam/scanning electron microscope (FIB/SEM) instrument using a Ga liquid metal ion source. A similar procedure was applied for all samples. Two or three lamellas were extracted from the same area in the middle part of the sample and attached to a Cu TEM grid. Lamella thinning was performed at 30 kV using 1 nA, 0.5 nA and 0.1 nA currents until electron transparency. At the end, lamella clean up steps were performed at 5 kV and 2 kV. In the case that a first TEM analysis indicated that the lamella was still relatively thick, the lamella was reloaded in the FIB and additional ion milling at 30 kV, 0.1 nA was applied.

The lamellas were analyzed in a JEOL JEM-ARM300F2 TEM equipped with a cold field emission gun as electron source and operating at 300 kV. The instrument can be operated in regular TEM mode as well as in scanning TEM mode. Defects were analyzed in TEM mode using classical bright field imaging. Cavities were revealed in out-of-focus bright field images. TEM cannot distinguish whether the cavities are empty (voids) or filled with gas (bubbles). Only for large cavities there is an indirect indication in the sense that spherical cavities are most likely pressurized bubbles, while faceted cavities are voids or under pressured bubbles. As the tungsten was only subjected to neutron irradiation and not exposed to H or He, there is no reason to assume that cavities will be filled with these elements. Therefore, the cavities are believed to be voids and they will be called so in this paper. The local thickness of the lamella was determined using convergent beam electron diffraction (CBED) patterns. In addition, A JEOL DUAL DRY SD 320 Energy dispersive X-ray spectroscopy (EDS) system is attached to the TEM. It has two windowless SDD detectors of 160 mm^2 surface. The TEM was operated in STEM mode to obtain detailed elemental maps.

3. Results

3.1. IGP tungsten

The grain structure of the material can be recognized in the backscattered electron (BSE) image in Fig. 2a. It consists of small grains of the order of a few micrometers elongated perpendicular to the surface. The grain structure agrees with the expected structure in IGP tungsten and the reported grain size in Table 1 with the plane normal to LD.

Fig. 2 shows the defect structure in the IGP grade tungsten. Typical radiation induced defects include dislocation loops and voids. The dislocation structure is revealed in the bright field image of Fig. 2b. A high number of elliptical features can be recognized that can be attributed to dislocation loops. Care needs to be taken with the interpretation of the contrast. The ion milling process introduces defects into the lamellas that are quite similar to the radiation induced dislocation loops. It is reasonable to assume that the loops introduced during the irradiation at high temperature have grown to a larger size than the FIB induced defects. The loop density was estimated based on this assumption, but it must be noted that the counting of the loops may be biased. Therefore, no error bar is given on the defect density. Considering these remarks, a loop density of 2.2 × 10^22/m^3 was obtained the IGP material.

The loops size distribution was constructed by analyzing about hundred loops and it is given in Fig. 2c. Most of the loops have a size in the range of 5–8 nm, but a significant fraction of the loops has grown to sizes above 10 nm and up to 20 nm. This results in an average loops size of (7.9 ± 3.5) nm, where the error bar is a measure of the width of the size distribution.

Voids are revealed in the out-of-focus images of Fig. 2d and e. The void density in the grain interior was compared to the voids near a grain boundary, but no significant differences could be noted. If a void depleted zone is present near the grain boundary, its width is <10 nm. The void density measured in this sample was (3.7 ± 1.0) × 10^22/m^3 and the void size, measured on 131 voids, was (4.3 ± 1.4) nm. The size distribution is given in Fig. 2f.

Table 1

Chemical composition and grain size of different tungsten grades [26]. The compositions of the commercial grades were provided by the manufacturer.

Materials	Major composition (by weight)	Equivalent diameter (μm)						
		Plane normal to*	W grain			Particle		
			D10	D50	D90	D10	D50	D90
IGP	Pure W (>99.97%)	ND	14.5	52.7	103.9	–	–	–
		LD	4.8	15.8	31.5	–	–	–
ALMT	Pure W (>99.97%)	ND	5.9	19.5	41.0	–	–	–
		LD	4.3	9.9	19.2	–	–	–
IGP-RX	Pure W (>99.97%)	–	31.7	60.4	108.4	–	–	–
W1TiC	99% W + 1% TiC	–	1.8	6.0	9.8	0.4	0.9	1.6
W2YO	98% W + 2% Y_2O_3	–	2.2	6.2	11.8	0.6	1.2	2.0

* ND: normal direction, LD: longitudinal direction.
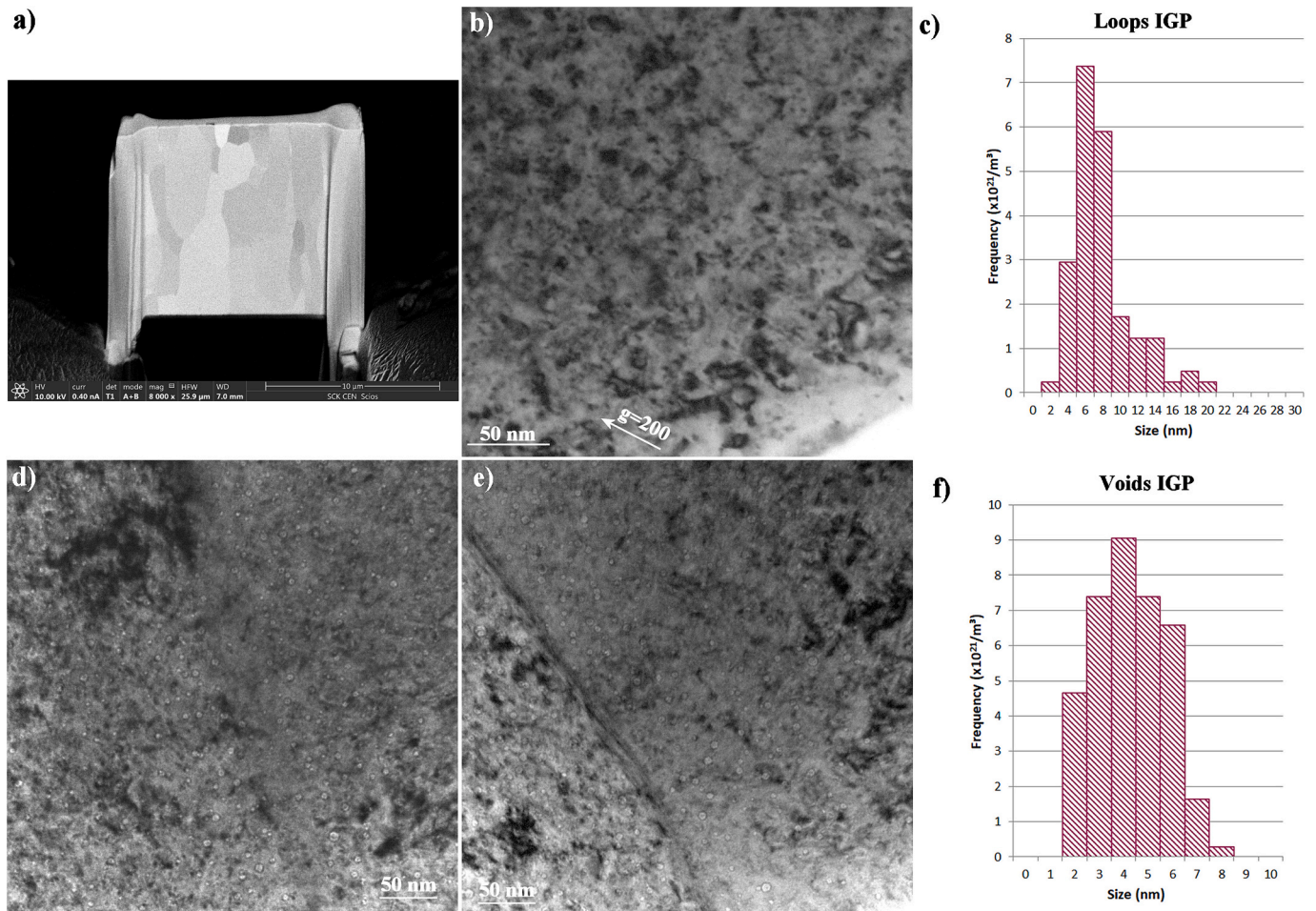
Fig. 2. a) BSE SEM image showing the grain structure of the IGP tungsten. b) Bright field image focusing on the radiation induced dislocation loops. c) Loops size distribution. d) and e) Under-focus images, with a defocus value of about 1 μm, revealing voids in the bulk and near a grain boundary. f) Voids size distribution.

3.2. Recrystallized IGP tungsten

The recrystallization treatment at 1600 °C resulted in a significant increase of the grain size. It is possible to extract a lamella from within a single grain, but for this study, the location of the lamella was chosen across a grain boundary. The BSE image in Fig. 3a reveals a grain boundary from the upper right to the lower left part of the lamella.

The dislocation loops are shown in the bright field image of Fig. 3b. Considering the potential confusion with FIB induced loops, the loops density was estimated to be $5.6 \times 10^{22}/m^3$. Loops have grown to large sizes of >20 nm, and it may even be possible that dislocation segments observed at the bottom of Fig. 3b are in fact loops that have grown >50 nm. No such segments were observed in the thicker part of the lamella, and it is not excluded that the proximity of a surface influenced the loop growth. These features were not added to the analysis of the loop size. On the other hand, many loops of smaller size were observed as well. This is reflected in the size distribution of Fig. 3c, where a double population of loops appears to be present. A first population has an average size around 6 nm, while the second population reaches a maximum around 12–13 nm. Including all, it leads to an average loop size, measured on 129 loops of (7.7 ± 4.0) nm, which is comparable to the not-recrystallized IGP tungsten.

The voids are shown in the under-focus images of Fig. 3d and e, in the grain interior and at the grain boundary respectively. The void density was measured to be $(2.4 \pm 1.0) \times 10^{22}/m^3$ and the void size, measured on 151 voids, was (4.8 ± 1.5) nm. The grain boundary in Fig. 3e was recorded edge-on. There appears to be a narrow band of about 10 nm wide with a lower void density. It indicates the presence of a small void depleted zone.

3.3. ALMT

In the BSE image of Fig. 4a, it can be observed that the ALMT grade tungsten has grains of similar size as the IGP tungsten, but with a more isomorphic shape. This observation agrees with the values reported in Table 1.

The dislocation loops are shown in the bright field image of Fig. 4b. The loops density was, considering the potential confusion with FIB induced loops, estimated to be $4.3 \times 10^{22}/m^3$. A fraction of the loops has grown to large sizes of >20 nm. On the other hand, many loops of smaller size were observed as well. This is reflected in the size distribution of Fig. 4d, where even three maxima appear to be present in the size distribution. A first population has an average size around 6 nm. A second population reaches a maximum around 11–12 nm. Only a small number of the largest loops was found, but they form a third population with a maximum around 21 nm. Including all, it leads to an average loop size of (8.9 ± 6.1) nm, measured on 128 loops.

The voids are shown in the under-focus bright field image of Fig. 4c and the size distribution is shown in Fig. 4e. The void density in this sample was $(2.8 \pm 0.5) \times 10^{22}/m^3$. the average void size, measured on 175 voids was (3.5 ± 1.3) nm.
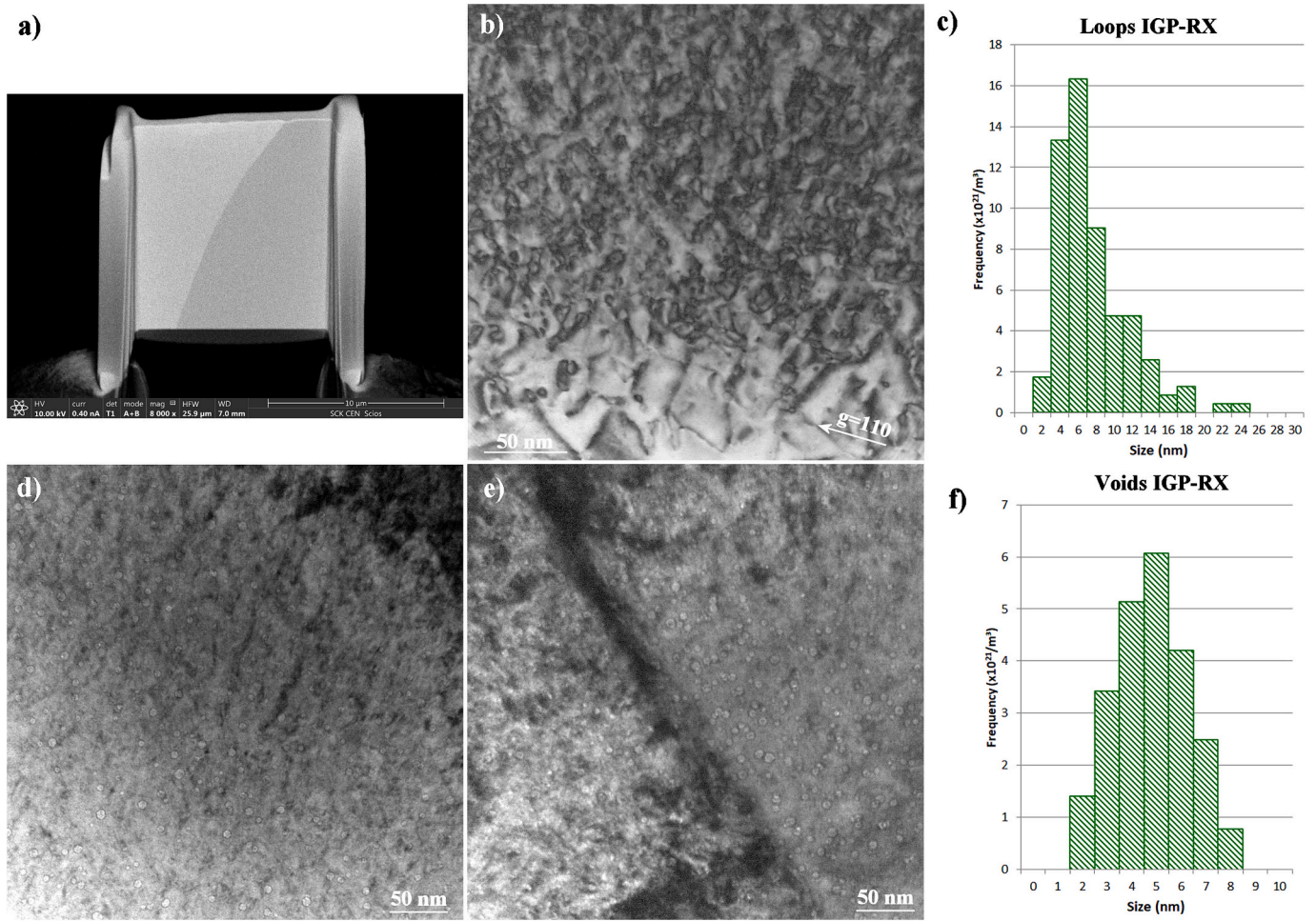
Fig. 3. a) BSE SEM image showing the grain structure of the recrystallized IGP tungsten. b) Bright field image focusing on the radiation induced dislocation loops. c) Loops size distribution. d) and e) Under-focus images, with a defocus value of about 1 μm, revealing voids in the bulk and near the grain boundary. f) Voids size distribution.

3.4. W2YO

An overview bright field image of the lamella extracted from the Y_2O_3 doped tungsten is shown in Fig. 5a. The spherical light gray areas are the Y_2O_3 particles. They are located in the grain interior as well as at the grain boundaries. No orientation relation was observed between the Y_2O_3 particles and the tungsten, neither at the grain boundaries nor in the grain interior, indicating that the particles are incoherent.

Fig. 5b focuses on the radiation induced dislocation loops. A high number of elliptical features can be observed that can be attributed to dislocation loops. The loop density was, considering the potential FIB induced defects, estimated to be $7.4 \times 10^{22}/m^3$. The size distribution measured on 120 loops, is represented in Fig. 5c. Even though a limited number of large loops are present, there are no clear signs of loop populations of different size. The average loop size is (8.4 ± 4.1) nm. Loops were also formed in the Y_2O_3 particles, and a few can be observed in Fig. 6b. The contrast agrees with loops formed on a {111} plane. The loops were not analyzed in further detail.

Voids were observed in the bulk tungsten (Fig. 5d) as well as in the Y_2O_3 grains (Fig. 5e). The measured voids densities are $(0.7 \pm 0.2) \times 10^{22}/m^3$ in the tungsten and $(11.0 \pm 1.0) \times 10^{22}/m^3$ in the Y_2O_3 grains. Moreover, as shown in Fig. 6a, a single large void of the order of 100 nm in size was observed in several Y_2O_3 grains. The void is faceted and has an octagon shape in projection on the (011) plane. The average void sizes are (3.4 ± 1.2) in W and (2.7 ± 0.8) nm in Y_2O_3, which means that the voids are, on average, larger in the W phase, but it is not sufficient to

end up with a comparable void volume fraction.

3.5. W1TiC

Fig. 7a shows an overview bright field image of a lamella extracted from the W1TiC material. The different phases were verified in a STEM-EDS analysis and the result is shown in Fig. 8. The lighter gray areas in the bright field image can be attributed to TiC particles. They are located at the grain boundaries as well as in the grain interior. It has been reported that the TiC particles have a semi-coherent interface with the tungsten where $[011]_{TiC}//[001]_W$ [33] and at least a partial coherency could be confirmed in the present TEM analysis. The porous grain indicated by the white arrow is different. Here the TiC particle reacted with oxygen forming titanium oxide instead. In the presented lamella, only one TiC grain had oxidized, but more were found at other locations.

Fig. 7b show a bright field image of the radiation induced dislocations loops. Within the limitation of the measurement, a loop density of $(4.6 \pm 0.5) \times 10^{22} /m^3$ was obtained. The loop size distribution is shown in Fig. 7c. It shows a single maximum around 7 nm with a tail towards larger loop sizes. The average loop size, measured on 132 loops was (9.8 ± 4.7) nm.

The void distribution is revealed in the under-focus images of Fig. 7d and e. It is quite different from the other tungsten materials. No voids were observed in the bulk tugnsten and in the TiC particles. Only at the grain boundaries or near the W-TiC interfaces a narrow band of voids is observed. The width of this band is of the order of 50 nm. The local void
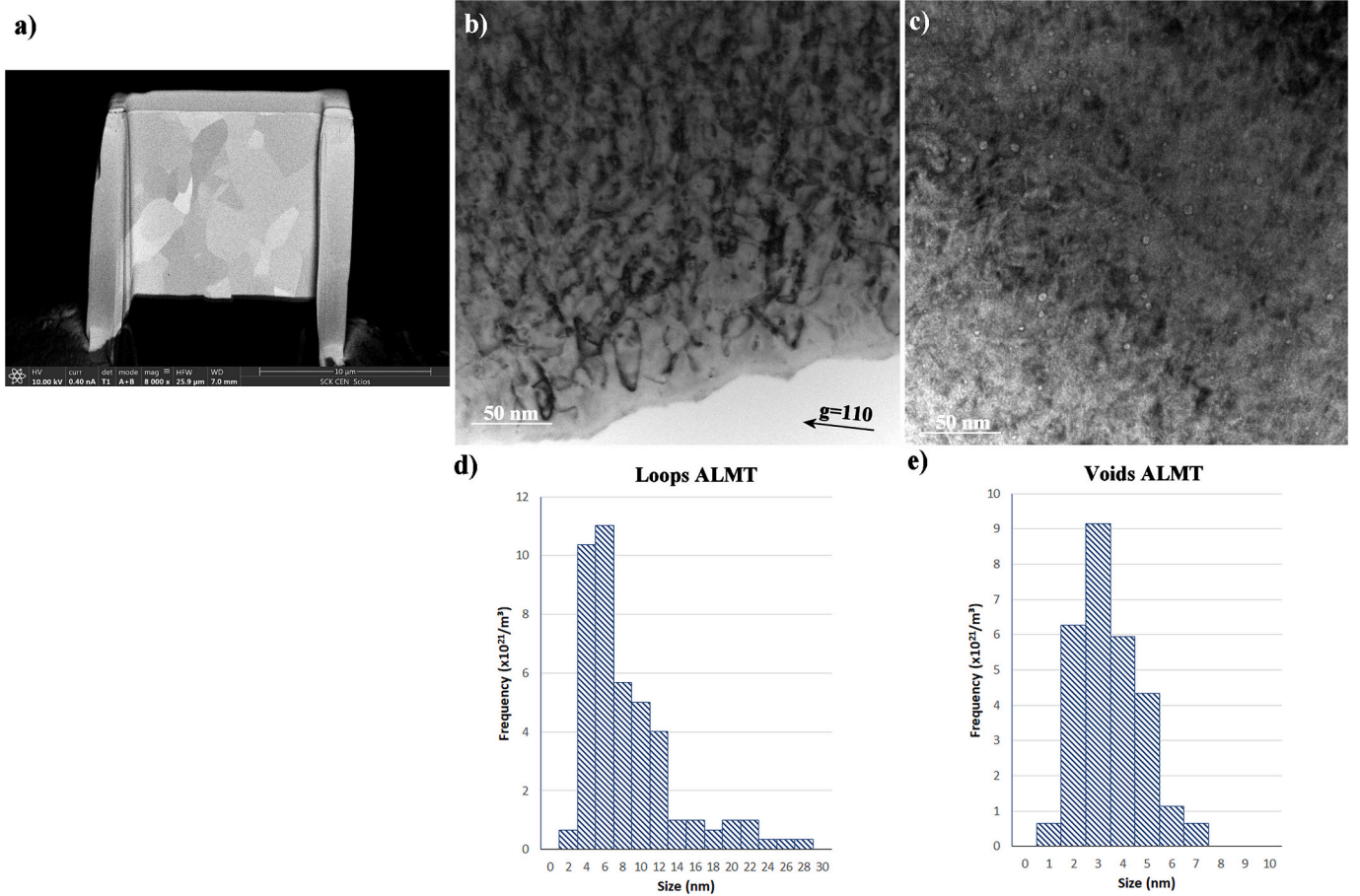
Fig. 4. a) BSE SEM image revealing the grain structure in ALMT grade tungsten. b) Bright field image showing the radiation induced dislocation loops. c) Under-focus image, with a defocus value of about 1 μm, reveling the presence of voids. d) and e) Size distributions of the loops and voids.

density in this narrow band equals 4.6×10^{22} $1/m^3$. The void size distribution is shown in Fig. 7f. It is comparable to the void sizes measured in the bulk of the other samples and an average size of (4.0 ± 1.4) nm was measured. The absence of voids in the bulk W does not exclude the presence of high amounts of vacancies, vacancy clusters or voids smaller than 1 nm, since these defects would not be resolved in the TEM images.

4. Discussion

Attempts were made to obtain information about the distribution of the transmuted Re and Os, as precipitation was reported by Klimenkov et al. under similar irradiation conditions [13]. Bright field images and selected area diffraction patterns were analyzed for small precipitates, which would appear as small dots in the bright field images or additional reflections in the diffraction patterns, but none could be identified. In addition, STEM EDS maps were recorded, also at higher magnification than in Fig. 7, but only homogeneously distributed Re and Os signals were obtained. The overlap of the M-peaks of W, Re and Os and an increase background at the location of the L-peaks by X-rays generated in the Cu grid, however, increase the detection limit of these elements and may have obscured the presence of small precipitates in the current analysis.

Application of the dispersed barrier model (DBM) to analyze the correlation between irradiation induced hardening and microstructure is a common approach in this kind of studies. The application of the DBM is a simple and convenient way to analyze contributions coming from different types of defects as was for example done by Hu et al. [34] for single crystal tungsten. The increase of the hardness, can be calculated as:

$$\Delta H_{calc} = 3.2 \, M \cdot \alpha \cdot \mu b \cdot (Nd)^{1/2} \tag{1}$$

Here, M = 3.06 [35], μ = 161 GPa, b = 0.274 nm (the Burgers vector of the moving line dislocation), N = the density of defects, and d = the mean size of the defects. α is a measure of the barrier strength and differs for loops voids and precipitates. Following Hu et al. [34], the dislocation loops are weak obstacles (with the barrier strength of 0.15, irrespective of its size), while the strength of the voids depends on the size, and it increases from 0.25 up to 0.4 as the void size increases from 1 to 2 nm up to 4 nm (and higher). To account for multiple types of barriers, the contributions to the hardening of each barrier are superimposed. Two limiting cases of superposition of the contributions can be considered, namely linear and squared superposition. Here, we have applied both linear and squared superposition rules to compare with the experimentally measured increase of the hardness ΔH_{exp}. The results of the calculations and the input taken for these calculations is given in Table 2 and Table 3, accordingly.

Given the calculated contributions coming from the loops (ΔH_{loops}) and voids (ΔH_{voids}) as presented in Table 2, the hardening induced by voids dominates in all the cases except W-Y$_2$O$_3$ where the void density in the bulk tungsten (for the voids resolved in TEM) was much lower than in the ITER grades. The fact that at high irradiation temperature the hardening is dominated by the voids is in agreement with the results of Hu et al. [34].

Secondly, one can see that for the ITER grades, the application of linear superposition yields to a total hardness that largely exceeds the experimental value, keeping in mind that some extra contribution coming from the non-resolved Re/Os precipitates was even not included. This is an argument in favor of using the squared superposition rule for
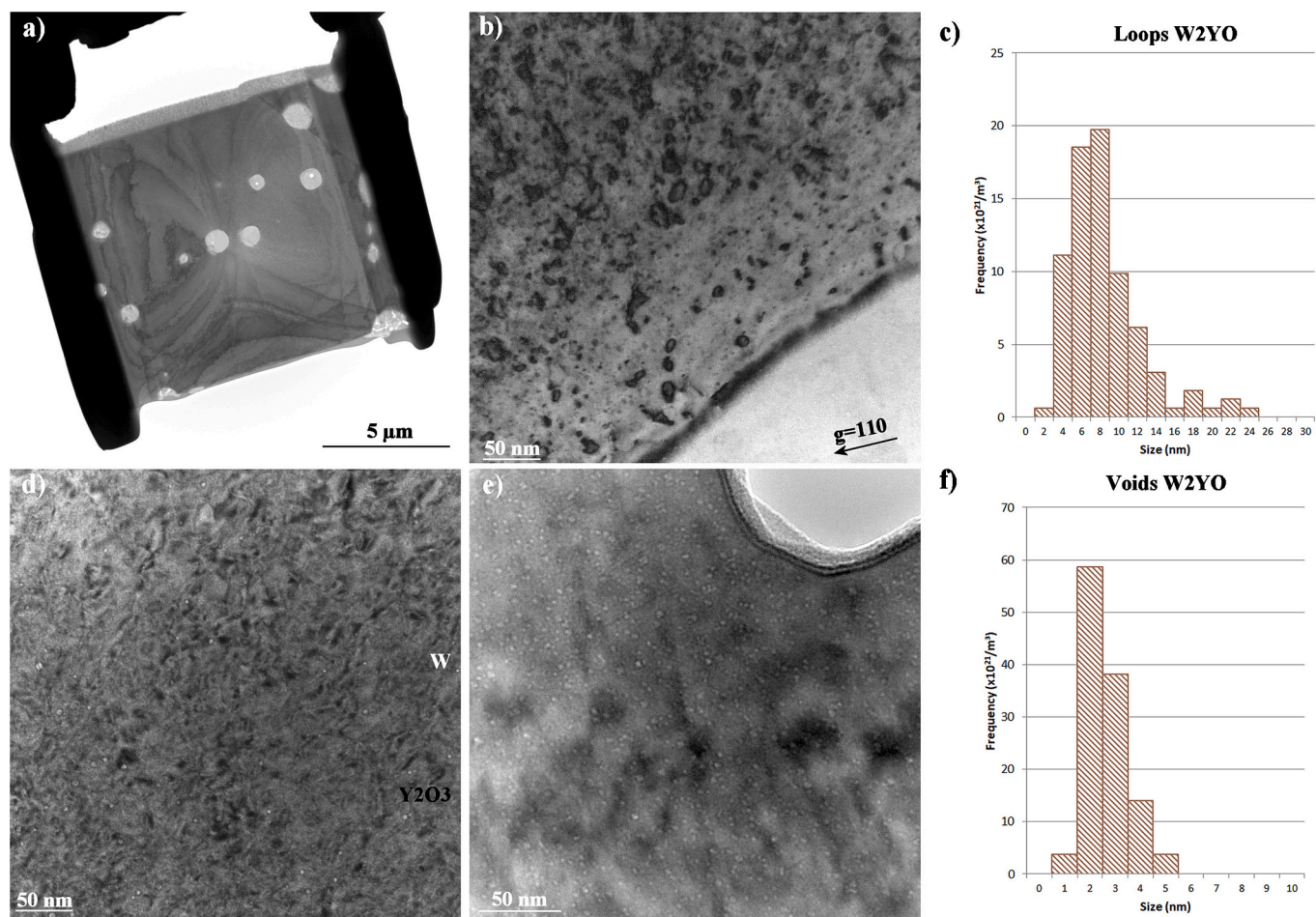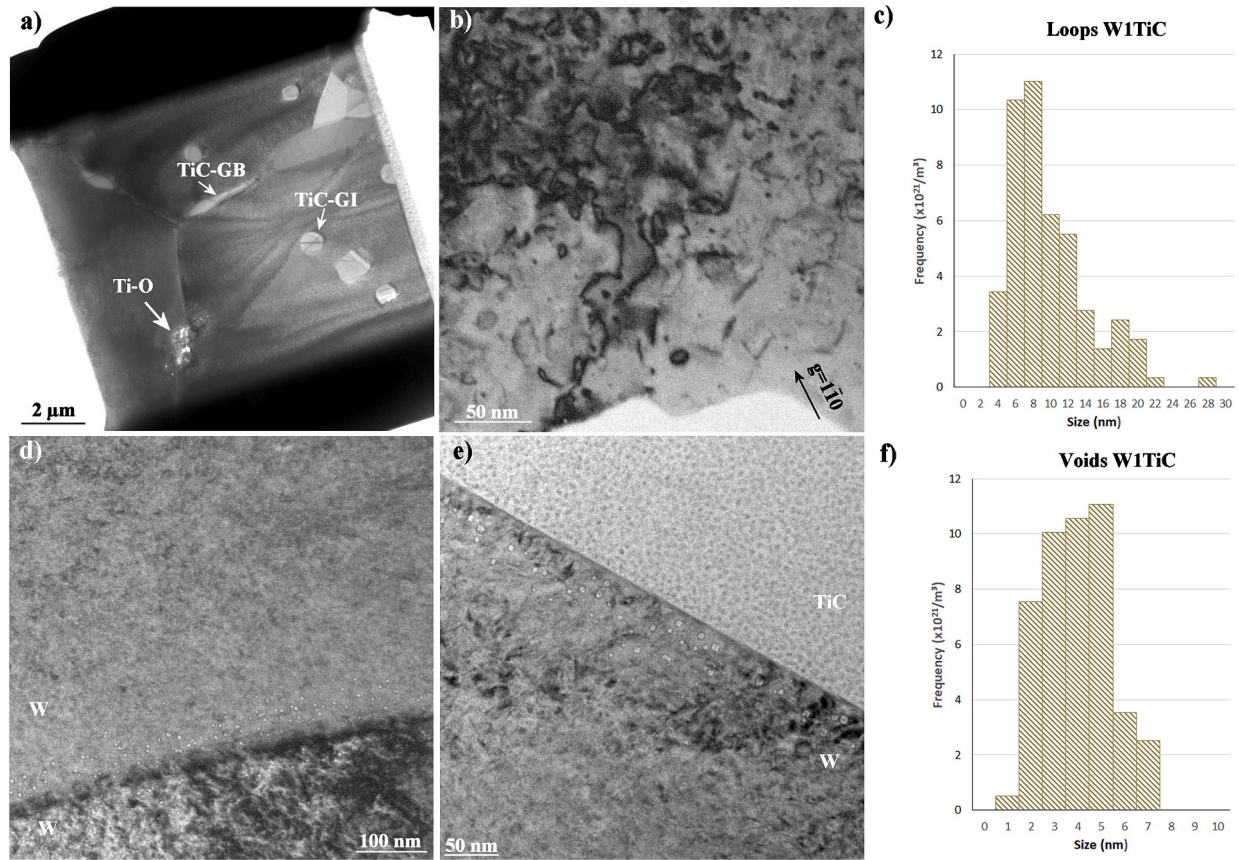
Fig. 5. a) Bright field image of the entire lamella prepared from the Y_2O_3 doped tungsten. b) Bright field image showing the presence of radiation induced dislocation loops. c) Loops size distribution. d) and e) Under-focus bright field images, with a defocus value of about 1 μm, revealing the presence of voids in tungsten and in the Y_2O_3 particle. f) Voids size distribution.
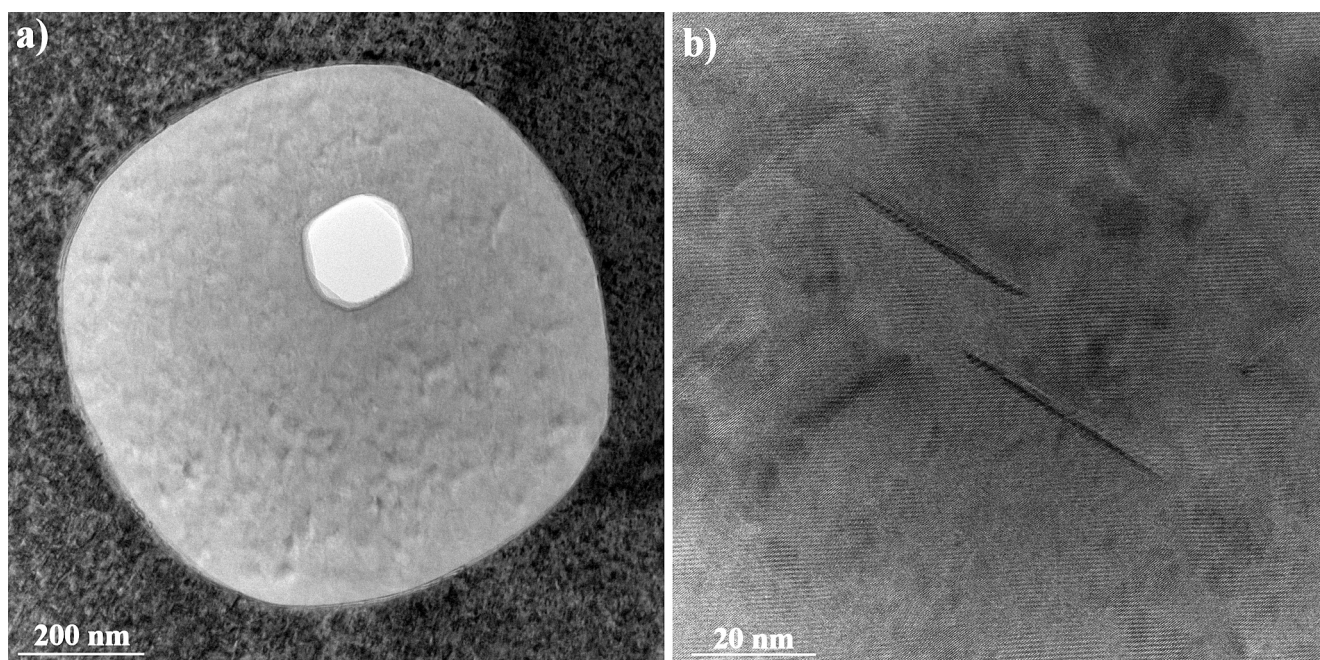

Fig. 6. a) Bright field image of a Y_2O_3 particle containing a large void and b) showing two dislocation loops.

Fig. 7. a) Bright field image of the entire lamella prepared from the W1TiC material. Ti-O indicates an oxidized TiC particle, TiC-GB is a TiC particle at a grain boundary and TiC-GI is a TiC particle in the grain interior. b) Bright field image showing the radiation induced dislocation loops. c) Loops size distribution. d) and e) Under-focus bright field images, with a defocus value of about 1 μm, near a tungsten – tungsten grain boundary and a tungsten – TiC interface. f) Voids size distribution.
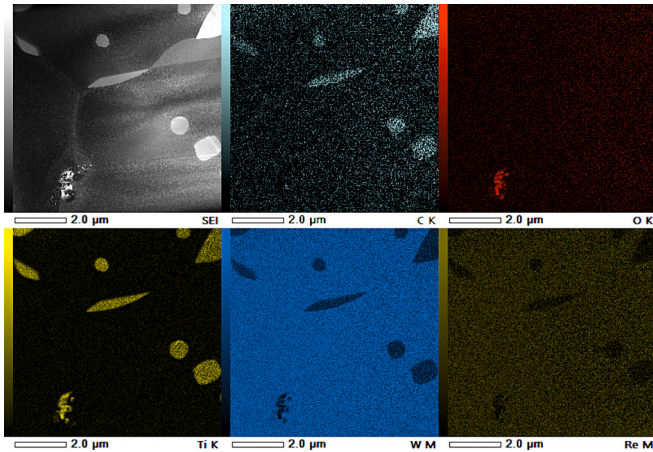
Fig. 8. Quantified STEM-EDS map of the W1TiC material showing the distribution of C, O, Ti, W and Re.

Table 2
Change of hardness measured in experiment and according to DBM i.e. ΔH_{calc} $3.2 \, M \cdot \alpha \cdot \mu b \cdot (Nd)^{1/2}$. The strength of the loops and voids were taken following Hu et al. [34]. α loops 0.15; α voids 0.4.

Sample ID, material	ΔH_{exp} [GPa]	ΔH_{loops} [GPa]	ΔH_{voids} [GPa]	ΔH_{calc} linear [GPa]	ΔH_{calc} squared [GPa]
IGP	1,73	0,84	2,14	2,98	2,30
IGP-RX	2,02	1,32	1,82	3,14	2,25
ALMT	2,9	1,24	1,68	2,92	2,09
W2YO	1,45	1,58	0,83	2,41	1,79
W1TiC	4,85	1,35	2,30	3,65	2,67

the evaluation of the hardening in this irradiation condition. However, even for the squared superposition rule, the total hardening exceeds the experimental value for IGP, IGP-RX and W2YO. Probably, a certain annealing of the initial microstructural defects in the material before irradiation (i.e. line dislocations, sub/low-angle grain boundaries, …) was induced by the high temperature irradiation so that the contribution of the initial defect structure to the total hardness is lower than before irradiation. To estimate the contribution of the initial defect structure to the hardness, the difference can be considered between the hardness of

non-irradiated IGP tungsten and single crystal tungsten, having no microstructural defects except dislocations induced by the indenter during the hardness test, which is 4.6–3.7 = 0.9 GPa [10]. The same difference between the IGP and IGP-RX grades is 0.8 GPa, which means that grain size has a larger impact on the hardness than the dislocation density. As the actual TEM measurements did not reveal signs of recrystallization and grain growth in IGP and ALMT samples, recovery is only expressed in a reduction of the dislocation density, which may not be sufficient to explain the difference between measurement and calculation. To further clarify this point, more detailed analysis is needed which would include both measurement of the dislocation density and precipitate size/density.

As for the advanced alloys, the measured irradiation-induced hardening in W2YO agrees rather well with the value calculated using the squared superposition method. In the case of W1TiC, although we provided the prediction of the DBM, the comparison is not adequate

Table 3
Microstructural information on the materials after irradiation to 1 dpa.

| Sample	Loop density ($\times 10^{22}$/ m^3)	Loop size (nm)	Void density ($\times 10^{22}$/ m^3)	Void size (nm)	Other comments
IGP	2.2	7.9 ± 3.5	3.7	4.3 ± 1.4	small sub-grains are present as in non-irradiated W. no sign of recrystallization.
IGP-RX	5.6	7.7 ± 4.0	2.4	4.8 ± 1.5	some very large loops are present
ALMT	4.3	8.9 ± 6.1	2.8	3.5 ± 1.3	small sub-grains are present as in non-irradiated W. no sign of recrystallization
W2YO	7.4	8.4 ± 4.1	0.7 in W 11.0 in Y$_2$O$_3$	3.4 ± 1.2 in W 2.7 ± 0.8 in Y$_2$O$_3$	no void depletion near GBs. No void depletion near Y$_2$O$_3$ interface, Loops and voids inside Y$_2$O$_3$ particle
W1TiC	4.6	9.8 ± 4.7	4.6	4.0 ± 1.4 nm	voids are observed only near grain boundaries.

because: (i) the contribution of large oxidized TiC particles is not accounted for (appropriate characterization of those particles was not possible given the dimension of the observation area and the complexity in the sample preparation techniques, likely EBSD study would be more appropriate for such types of defects); (ii) there is a strong heterogeneity in the location of voids, so the application of DBM is questionable by its nature. However, if one would account for the contribution from voids as if these are present homogeneously over the matrix, even then the total hardness increase is far smaller than the experimentally measured value, which indeed confirms a large contribution from the oxidized TiC precipitates.

The graphical comparison of the mean size and density of the loops and voids is given in Fig. 9. One can see that there is no essential difference in the microstructure observed in IGP, ALMT and IGP-RX. The recrystallization leads to a reduction of the void density and increase of the loop density. Such effect could be explained assuming that dislocation lines and low-angle grain boundaries, the main intrinsic defects in as-forged IGP and ALMT, act as sinks for the mobile loops, while these intrinsic defects are nearly missing in the IGP-RX and this is why the density of the remaining loops is up to a factor 3 higher.

In the W2YO material, the incoherent interface between the Y$_2$O$_3$ particle and the W matrix provides additional sinks for radiation

induced defects. In addition, the density of voids registered in the Y$_2$O$_3$ particle is one order of magnitude larger than in the W matrix, while the mean void size is nearly the same (3.4 nm in W vs. 2.7 nm in Y$_2$O$_3$). This is a striking result, because it shows that in the investigated conditions the susceptibility of Y$_2$O$_3$ to the void swelling is much larger than that of tungsten. In addition to the spherical nano-voids, huge octagon-shaped cavities were observed (see Fig. 6a) with a size of 100–200 nm. Also, the formation of dislocation loops (see Fig. 6b) was registered, which are likely the defects formed by the self-interstitials. Although, one needs further investigation of the structure and morphology of the defects inside Y$_2$O$_3$ particles, the currently obtained results are promising as they show that Y$_2$O$_3$ particles indeed act as sinks for the irradiation defects in the W matrix and effectively reduce the density of the voids in the matrix. Moreover, the measured reduction of the defect density in W matrix correlates well with the smallest increase of the hardness compared to other studied grades (see Fig. 1).

Finally, we come to the discussion of W-TiC. The addition of coherent TiC particles to tungsten leads to grain refinement, improved ductility and reduction of neutron irradiation induced hardening [33]. However, under the irradiation conditions applied here, the material shows a significant increase of the hardening at 1200 °C irradiation temperature, whereas the higher irradiation temperature leads to a hardness decrease in the other alloys. The coherence of the TiC particles is reported to resist neutron irradiation and also under the irradiation conditions applied here, at least partial coherence was noted. A striking feature is the fact that no voids were observed in W bulk and in the TiC particles, while dislocation loops were observed readily. The only location where voids were observed were the near-grain boundary regions or at the W-TiC interface, the width of this void-rich layer is about 50 nm. In addition, some porous structures of several μm in size were identified even at the stage of FIB lamellae preparation. Only one of such structure was registered per lamella, which means that more material needs to be analyzed to obtain an accurate number density. Those porous structures are tentatively attributed to the internal oxidation of TiC particles forming oxides. The origin for the formation of such oxides must come from the material itself, because all other studied samples were irradiated in the same holder face-to-face, and no surface oxidation was identified after the irradiation on or inside other samples. Accordingly, we can assume that the dissolved oxygen, stored during the production and sintering of the material, was released from its lattice or chemical traps due to the high temperature irradiation and this caused the transformation of small TiC precipitates into larger Ti-C-O particles. Given that the W-TiC material was sintered at 2400 °C and TiC particles were stable, the neutron irradiation coupled with high temperature somehow triggered this process of internal oxidation, while a simple
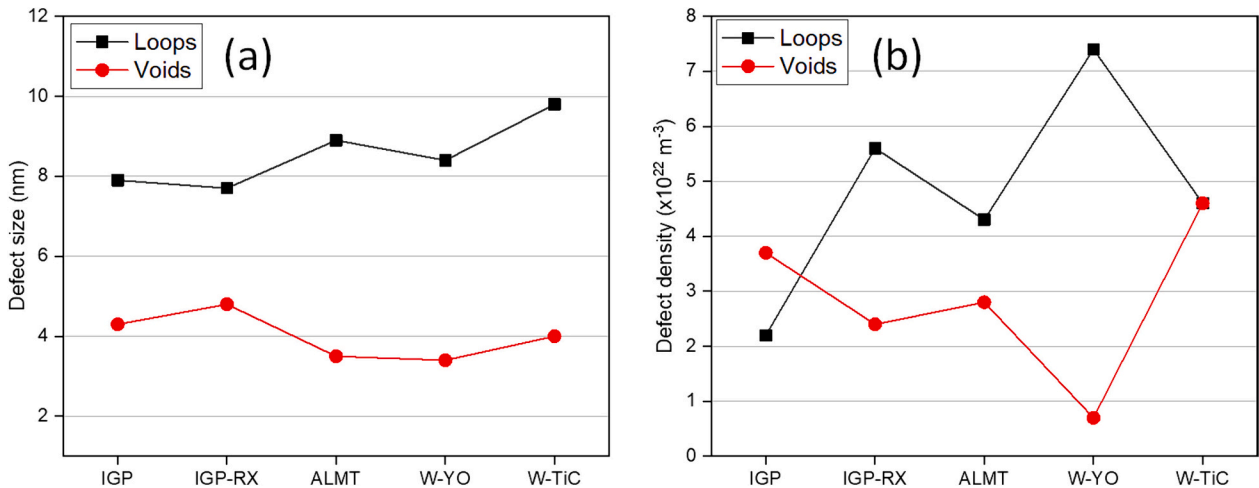
Fig. 9. (a) Mean size of dislocation loops and voids; (b) density of dislocation loops and voids.

thermal annealing at 1200 °C turned out not to be sufficient.

5. Conclusions

Based on the presented results and discussion, we can provide the following concluding statements:

1. Based on the measured dislocation loop and void size/density distributions and by applying the dispersed barrier hardening model one cannot provide a comprehensible explanation for the difference in the irradiation-induced hardness in IGP and ALMT materials, which are both ITER specification grades with comparable purity, nominal microstructure and mechanical properties. The difference might be ascribed to a contribution coming from Re/Os precipitates or some segregation of Re/Os at irradiation defects.

2. Based on the measured dislocation loop and void size/density distributions for IGP in the as-received and in the recrystallized state (i. e. IGP-RX), one can conclude that the removal of sub-grains and the reduction of the dislocation density due to recrystallization has an insignificant impact on the accumulation of loops and voids at 1 dpa and T_{irr} = 1200 °C. In line with this observation, there is only a minor difference in the irradiation-induced hardness increase.

3. The lowest irradiation-induced hardening was realized in the W2YO grade, which is consistent with the calculated hardening according to the DBM based on the measured loop/void size/density distributions. This might serve as supporting evidence of the grain refinement concept which helps to reduce the embrittlement under high irradiation temperature conditions.

4. The TEM inspection of W1TiC material did not reveal an excessively high density of loops or voids, that could explain the irradiation hardening. On the contrary, the void density was lower in this material as compared to the others investigated here. Hence, the extraordinary hardness increase in W-TiC cannot be explained by the matrix damage resolvable by TEM. However, at least a part of this extra hardening could be explained by the transformation of TiC precipitates into Ti oxides. We speculate that the dissolved oxygen, stored during the production and sintering of the material, was released from its traps due to the high temperature irradiation and converted part of the small TiC precipitates into larger titanium oxides. We highlight the role of the irradiation involved in this process, because the sintering of the material was performed at 2400 °C and, therefore, a simple thermal annealing at 1200 °C should not be sufficient. The suppression of the large void formation could also be related to the oxygen which may act to stabilize/bind small vacancy clusters causing their high density at a size that is not yet resolvable in TEM.

5. The performed TEM analysis did not allow to resolve Re/Os precipitates in the studied samples, however, their presence in the material is undoubtful given the recent investigations done on similar samples irradiated in the same conditions. The reasons for the failure to resolve the precipitates were discussed.

CRediT authorship contribution statement

W. Van Renterghem: Investigation, Formal analysis, Writing – original draft. **K. Iroc:** Writing – original draft. **D. Terentyev:** Writing – original draft, Conceptualization. **S. Antusch:** Resources. **M. Rieth:** Resources.

Declaration of competing interest

The authors declare that they have no known competing financial interests or personal relationships that could have appeared to influence the work reported in this paper.

Data availability

Data will be made available on request.

References

[1] S.J. Zinkle, Fusion materials science: overview of challenges and recent progress, Phys. Plasmas 12 (5) (2005) 058101.

[2] S. Matsuda, K. Tobita, Evolution of the ITER program and prospect for the next-step fusion DEMO reactors: status of the fusion energy R&D as ultimate source of energy, J. Nucl. Sci. Technol. 50 (4) (2013) 321–345.

[3] M. Rieth, D. Armstrong, B. Dafferner, S. Heger, A. Hoffmann, M. Hoffmann, et al., Tungsten as a structural divertor material, Adv. Sci. Tech. 73 (2010) 11–21.

[4] V. Chatzikos, K. Mergia, G. Bonny, D. Terentyev, D. Papadakis, G.E. Pavlou, S. Messoloras, Positron annihilation spectroscopy investigation of defects in neutron irradiated tungsten materials, Int. J. Refract. Met. Hard Mater. 105 (2022) 105838.

[5] S.J. Zinkle, Advanced materials for fusion technology, Fus. Eng. Design 74 (1–4) (2005) 31–40.

[6] G. Pintsuk, Tungsten as plasma facing material, Comprehensive Nucl. Mater. 4 (2012) 551–581.

[7] A. Giannattasio, Z. Yao, E. Tarleton, S.G. Roberts, Brittle–ductile transitions in polycrystalline tungsten, Philos. Mag. 90 (2010) 3947–3959.

[8] B. Gludovatz, S. Wurster, A. Hoffmann, R. Pippan, Fracture toughness of polycrystalline tungsten alloys, Int. J. Refract. Met. Hard Mater. 28 (6) (2010) 674–678.

[9] T. Hirai, S. Panayotis, V. Barabash, C. Amzallag, F. Escourbiac, A. Durocher, M. Merola, J. Linke, Th. Loewenhoff, G. Pintsuk, M. Wirtz, I. Uytdenhouwen, Use of tungsten material for the ITER divertor, Nucl. Mater. Energy 9 (2016) 616–622.

[10] D. Terentyev, C. Yin, A. Dubinko, C.C. Chang, J.H. You, Neutron irradiation hardening across ITER diverter tungsten armor, Int. J. Refract. Met. Hard Mater. 95 (2021) 105437.

[11] A. Dubinko, D. Terentyev, C. Yin, W. Van Renterghem, B. Rossaert, M. Rieth, et al., Microstructure and hardening induced by neutron irradiation in single crystal, ITER specification and cold rolled tungsten, I Int, J. Refract. Met. Hard Mater. 98 (2021) 105522.

[12] E. Gaganidze, A. Chauhan, H.C. Schneider, D. Terentyev, G. Borghmans, J. Aktaa, Fracture-mechanical properties of neutron irradiated ITER specification tungsten, J. Nucl. Mater. 547 (2021) 152761.

[13] M. Klimenkov, M. Durrschnabel, U. Jantsch, P. Lied, M. Rieth, H.C. Schneider, D. Terentyev, W. Van Renterghem, Microstructural analysis of W irradiated at different temperatures, J. Nucl. Mater. 572 (2022) 154018.

[14] M. Klimenkov, U. Jantsch, M. Rieth, H.C. Schneider, D.E.J. Armstrong, J. Gibson, S. G. Roberts, Effect of neutron irradiation on the microstructure of tungsten, Nucl. Mater. Energy 9 (2016) 480–483.

[15] X.X. Hu, C.M. Parish, K. Wang, T. Koyanagi, B.P. Eftink, Y. Katoh, Transmutation-induced precipitation in tungsten irradiated with a mixed energy neutron spectrum, Acta Mater. 165 (2019) 51–61.

[16] D. Papadakis, S. Dellis, K. Mergia, V. Chatzikos, D. Terentyev, G. Bonny, et al., The competing effects of temperature and neutron irradiation on the microstructure and mechanical properties of ITER grade tungsten, Fusion Eng. Des. 168 (2021) 112608.

[17] D. Terentyev, M. Rieth, G. Pintsuk, J. Riesch, A. von Muller, S. Antusch, et al., Recent progress in the assessment of irradiation effects for in-vessel fusion materials: tungsten and copper alloys, Nucl. Fusion 62 (2) (2022) 026045.

[18] M. Duerrschnabel, M. Klimenkov, U. Jaentsch, M. Rieth, H.C. Schneider, D. Terentyev, New insights into microstructure of neutron-irradiated tungsten, Sci. Rep. UK 11 (1) (2021) 7572.

[19] A. Chauhan, Q. Yuan, D. Litvinov, E. Gaganidze, H.C. Schneider, D. Terentyev, J. Aktaa, Effect of temperature on the neutron irradiation-induced cavities in tungsten, Philos. Mag. 102 (17) (2022) 1665–1683.

[20] S. Nogami, A. Hasegawa, M. Fukuda, S. Watanabe, J. Reiser, M. Rieth, Tungsten modified by potassium doping and rhenium addition for fusion reactor applications, Fusion Eng. Des. 152 (2020) 111445.

[21] S. Antusch, D. Armstrong, B. Britton, L. Commin, J. Gibson, H. Greuner, et al., Mechanical and microstructural investigations of tungsten and doped tungsten materials produced via powder injection molding, Nucl. Mater. Energy 3-4 (2015) 22–31.

[22] X.D. Yang, Z.M. Xie, S. Miao, R. Liu, W.B. Jiang, T. Zhang, et al., Tungsten-zirconium carbide-rhenium alloys with extraordinary thermal stability, Fusion Eng. Des. 106 (2016) 56–62.

[23] S. Wurster, N. Baluc, M. Battabyal, T. Crosby, J. Du, C. Garcia-Rosales, et al., Recent progress in R&D on tungsten alloys for divertor structural and plasma facing materials, J. Nucl. Mater. 442 (1–3) (2013) S181–S189.

[24] C. Yin, D. Terentyev, T. Pardoen, A. Bakaeva, R. Petrov, S. Antusch, et al., Tensile properties of baseline and advanced tungsten grades for fusion applications, Int. J. Refract. Met. Hard Mater. 75 (2018) 153–162.

[25] C. Yin, D. Terentyev, T. Zhang, S. Nogami, S. Antusch, C.C. Chang, R.H. Petrov, T. Pardoen, Ductile to brittle transition temperature of advanced tungsten alloys for nuclear fusion applications deduced by miniaturized three-point bending tests, I Int, J. Refract. Met. Hard Mater. 95 (2021) 105464.

[26] C. Yin, D. Terentyev, A. Dubinko, T. Zhang, M. Wirtz, S. Antusch, R.H. Petrov, T. Pardoen, Impact of neutron irradiation on hardening of baseline and advanced tungsten grades and its link to initial microstructure, Nucl. Fusion 61 (6) (2021).

[27] M. Wirtz, J. Linke, T. Loewenhoff, G. Pintsuk, I. Uytdenhouwen, Thermal shock tests to qualify different tungsten grades as plasma facing material, Phys. Scr. T167 (2016) 014015.

[28] S. Nogami, A. Hasegawa, M. Fukuda, S. Watanabe, J. Reiser, M. Rieth, Tungsten modified by potassium doping and rhenium addition for fusion reactor applications, Fusion Eng. Des. 152 (2020) 111445.

[29] A. Stankovskiy, G. Van den Eynde, L. Fiorito, ALEPH V.2.7, A Monte Carlo Burn-Up Code, SCK CEN, 2018.

[30] JEFF Scientific Working group, The Joint Evaluated Fission and Fusion Nuclear Data Library, JEFF-3.3, Nuclear Energry Agency, 2017.

[31] D.A. Brown, M. Chadwick, R. Capote, A. Kahler, A. Trkov, M. Herman, A. Sonzogni, Y. Danon, A. Carlson, M. Dunn, ENDF/B-VIII. 0: the 8th major release of the nuclear reaction data library with CIELO-project cross sections, new standards and thermal scattering data, Nuclear Data Sheets 148 (2018) 1–142.

[32] A.Y. Konobeyev, U. Fischer, Y.A. Korovin, S. Simakov, Evaluation of effective threshold displacement energies and other data required for the calculation of advanced atomic displacement cross-sections, Nucl. Energy Techn. 3 (3) (2017) 169–175.

[33] H. Kurishita, Y. Amano, S. Kobayashi, K. Nakai, H. Arakawa, Y. Hiraoka, T. Takida, K. Takebe, H. Matsui, Development of ultra-fine grained W–TiC and their mechanical properties for fusion applications, J. Nucl. Mater. 367–370 (2007) 1453–1457.

[34] X.X. Hu, T. Koyanagi, M. Fukuda, N.A.P.K. Kumar, L.L. Snead, B.D. Wirth, Y. Katoh, Irradiation hardening of pure tungsten exposed to neutron irradiation, J. Nucl. Mater. 480 (2016) 235–243.

[35] R.E. Stoller, S.J. Zinkle, On the relationship between uniaxial yield strength and resolved shear stress in polycrystalline materials, J. Nucl. Mater. 283 (2000) 349–352.